Journal Pre-proof

Site-selective laser spectroscopy and defect configurations of the Nd^{3+}-Li^{+} centres in ZnO powders

N.C. Gatsi, M. Mujaji, D. Wamwangi, R.A. Jackson

PII: S0925-8388(19)34552-9

DOI: https://doi.org/10.1016/j.jallcom.2019.153306

Reference: JALCOM 153306

To appear in: *Journal of Alloys and Compounds*

Received Date: 6 October 2019

Revised Date: 4 December 2019

Accepted Date: 5 December 2019

Please cite this article as: N.C. Gatsi, M. Mujaji, D. Wamwangi, R.A. Jackson, Site-selective laser spectroscopy and defect configurations of the Nd^{3+}-Li^{+} centres in ZnO powders, *Journal of Alloys and Compounds* (2020), doi: https://doi.org/10.1016/j.jallcom.2019.153306.

CRediT author statement

Nyepudzai C. Gatsi: Investigation, formal analysis, writing - original draft, writing - review and editing

Marjorie Mujaji: Conceptualization, validation, formal analysis, writing - review and editing, resources, supervision, funding acquisition

Daniel Wamwangi: Formal analysis, writing - review and editing, supervision

Robert A. Jackson: Software, formal analysis, resources, writing - review and editing

Site-selective laser spectroscopy and defect configurations of the Nd^{3+}-Li^{+} centres in ZnO powders

N. C. Gatsi [a,b], M. Mujaji [a], D. Wamwangi [a], R. A. Jackson [c]

[a] *School of Physics and DST/NRF Centre of Excellence in Strong Materials, University of the Witwatersrand, Johannesburg. Private Bag 3, Wits 2050, South Africa*

[b] *African Materials Science and Engineering Network (AMSEN), A Carnegie – IAS RISE Network*

[c] *Lennard-Jones Laboratories, School of Chemical and Physical Sciences, Keele University, Keele, Staffordshire ST5 5BG, UK*

E-mail: Nyepudzai.Gatsi1@students.wits.ac.za

Abstract

Near-infrared emission in the 885 – 915 nm region was observed for two distinct Nd^{3+} centres that co-exist in hexagonal wurtzite ZnO:1mol%Nd^{3+}:10mol%Li^{+} powders. The powder samples were prepared by sintering in air at 950 □ and the emission, attributed to the $^4F_{3/2} \rightarrow {}^4I_{9/2}$ transitions of Nd^{3+} ions, was measured in the 10 – 75 K temperature range. The sharp and well-resolved Nd^{3+} emission transitions are present in Nd^{3+}-Li^{+} co-doped samples only, and the intensity increases with Li^{+} concentration. X-ray diffraction, scanning electron microscopy and energy dispersive spectroscopy were used for structural, morphology and compositional assessments of the samples. Atomistic modelling using GULP shows two favourable Nd^{3+}-Li^{+} substitutional positions, in consistence with the experimental findings.

Keywords: site-selective spectroscopy; Nd^{3+}-Li^{+}; ZnO powders; modelling; defect configurations; crystal-field levels.

1. Introduction

In the last decade, a variety of ZnO materials doped with trivalent rare-earth ions (RE^{3+}) have received renewed research attention [1-8] due to their potential impact in several applications, such as in the production of white light [6] and in photocatalysis [8]. Although there are incorporation challenges due to the differences in ionic radii between the Zn^{2+} ion (74.0 pm) and the RE^{3+} ions (84.8 – 103.4 pm) [9], the highly favourable characteristics of the wurtzite ZnO sustain the research interest. This is largely because of the multiple RE^{3+} energy-level states which lie within the wide band gap of ZnO (3.44 eV at 10 K) [10]. ZnO has other merits, including high transparency in the visible and near-infrared regions, availability in abundance, non-toxicity, high radiation hardness and the high melting temperature of 2 248 K [10]. Due to these unique properties, ZnO has found applications in solar cells, supercapacitors, UV photodetectors, photodiodes and sensors [11].

Optical emission and absorption spectra of RE^{3+} ions comprise spectral lines which vary weakly with the host matrix, as a result of shielding of the 4*f* electrons by the fully-occupied $5s^2$ and $5p^6$ shells [12]. Further, the intra-4*f*-shell transitions are sensitive to the local symmetry at the RE^{3+} site in the host matrix, hence a variety of optically-active centres with different site symmetries can be stable in a given host matrix. Optical spectroscopic studies of trivalent rare-earth ions in the ZnO matrix can be performed with either indirect or direct laser excitation. Indirect laser-excitation processes rely on relatively high concentration of the RE^{3+} dopant (extrinsic defects) as well as intrinsic ZnO defects such as zinc and

oxygen vacancies, antisites and interstitials. For this excitation mechanism, the incoming laser radiation is absorbed by the intrinsic defects and then some or all of the energy is subsequently transferred to the RE^{3+} ions through their interaction with the intrinsic defects. The interaction and energy transfer manifest in the observation of characteristic RE^{3+} emission spectra without any distinction between the variety of RE^{3+} centres that could be involved. Direct excitation on the other hand, uses incident resonance radiation to excite a specific transition resulting in centre-specific emission spectra which, by the site-selective excitation technique, enables distinction between the variety of RE^{3+} centres present in a given host [12].

Nd^{3+} is by far the most utilised optical medium in solid state lasers while the historical hosts are mainly garnets [13]. Given the proven lasing capabilities of Nd^{3+} ions and the uniquely favourable characteristics of ZnO, optical activity in ZnO:Nd^{3+} would provide versatile and robust optical and opto-electronic devices for technological and scientific as well as medical applications, hence the choice for the present study. Lithium has already been identified as a highly favourable co-dopant for RE^{3+}-ion charge compensation in the ZnO lattice; additional attributes include improved crystallinity and increased grain size of the powder material [14]. In the recent past [2,3], emission and absorption profiles of Nd^{3+} ions doped into ZnO powders have been recorded at room temperature [2] as well as at 10 K [3] and 4.2 K [2] using UV [3], visible [3] and near-infrared excitation-wavelengths [2]. The UV wavelength used (370 nm) leads to ZnO inter-band absorption transitions while the visible and infrared excitation wavelengths (604 nm and 811 nm) are resonant with Nd^{3+} absorption transitions. However, the direct excitations also resulted in complex emission profiles which were attributed to presence of a variety of Nd^{3+} centres in the samples, but no distinction of the centres was made.

In the work presented here, the technique of site-selective laser spectroscopy is applied to ZnO:1mol%Nd^{3+}:10mol%Li^{+} powders in order to separately record the emission and excitation spectra of the two different Nd^{3+} centres present and consider the nature of each centre. Studies were conducted at sample temperatures in the 10 – 75 K range, firstly using the 457.9 nm Ar^{+} laser line to excite the Nd^{3+} ions indirectly through energy transfer processes and then by directly populating the D ($^2G_{7/2}$;$^4G_{5/2}$) multiplet of Nd^{3+} ions near 600 nm using a tunable dye laser. Nd^{3+} ions yield dominant emission near 1 060 and 890 nm [2,3], which is attributed to the $^4F_{3/2} \rightarrow {}^4I_{11/2}$ and $^4F_{3/2} \rightarrow {}^4I_{9/2}$ transitions, irrespective of the higher-lying multiplet that is excited. Emission transitions to the first excited multiplet ($^4F_{3/2} \rightarrow {}^4I_{11/2}$) were not accessible with the GaAs detector available for this work. Energy levels for the three accessible multiplets ($^4I_{9/2}$, $^4F_{3/2}$ and $^2G_{7/2}$;$^4G_{5/2}$) are presented together with the $^4F_{3/2}$ multiplet life-time, for each centre. In addition, we report modelling calculations of configurations of Nd^{3+} and charge compensating Li^{+} ions in the ZnO lattice. The results presented here are a significant contribution to the characterization of rare-earth defects in ZnO. Understanding of such fundamental characteristics of the optically-active material is invaluable for potential applications in devices such as near-infrared solid state lasers, solar cells and light emitting diodes. Another potential application is in biological imaging since biological tissues are highly transparent in the same near-infrared regions where Nd^{3+} emission occurs [3].

2. Materials and methods

2.1 Sample preparation: ZnO:1mol%Nd^{3+}:10mol%Li^{+} powder samples were prepared from research-grade ZnO (99.999%), Nd_2O_3 (99.9%) and Li_2CO_3 (99.997%) obtained from Sigma-Aldrich. Required masses of the constituent compounds were mixed and hand-ground in an agate mortar for 2 h. For each sample, 0.4 g of ground powder was compacted into a 'green body' pellet, using a moulding die and a uniaxial Specac hydraulic press uniaxially loaded to 4 tonnes. The pellet was then sintered at 950 □, in air, using a ramping rate of 5 ℃ per minute followed by a 2-hour dwell time at the sintering temperature (950 □). The sample was allowed to cool down to room temperature naturally before removal from the furnace. For reference, undoped ZnO, ZnO:1mol%Nd^{3+} and ZnO:10mol%Li^{+} samples were also prepared in the same way.

2.2 Structure and morphology characterization: Powder X-ray diffraction (PXRD) patterns were collected using a Bruker AXS D2 Phaser desktop diffractometer equipped with a Co $K\alpha_1$ radiation (λ = 0.197 nm) source. Crystalline phases of the powders were identified and lattice parameters determined from the matching diffraction patterns and least squared fitting of the peak positions, respectively. A Zeiss GeminiSEM system equipped with an energy dispersive spectroscopy (EDS) capability was used to investigate the topological, morphological and compositional information of the top surface layer of the samples.

2.3 Photoluminescence (PL) studies: For indirect excitation of the Nd^{3+} ions, the 457.9 nm wavelength radiation from a Spectra-Physics 2080 Ar^{+} laser, was directed onto the sample which was mounted onto the cold finger of a Janis CCS-150 closed-cycle cryostat. The temperature of the sample was set to 10 K as monitored by a LakeShore temperature controller. Fluorescence from the surface layer of the sample was directed into a McPherson monochromator (model 2062DP) and detected by a high responsivity GaAs photomultiplier tube (PMT) cooled to -40 □ and operated at -1350 V. The PMT output was channelled to a photon counter through a single stage pre-amplifier. Slit widths of 500 μm, scanning step sizes of 0.5 nm and an integration time of 4.0 s were used to record the spectra. For site-selective excitation studies, a Spectra-Physics dye laser with a continuous flow of Rhodamine 590 dye which is tunable in the 570 – 640 nm range, was pumped with the 514.5 nm Ar^{+}-laser line and the output beam directed onto the sample. Specific wavelengths of the dye-laser emission matching particular $^2G_{7/2}$;$^4G_{5/2} \rightarrow {}^4I_{9/2}$ (~ 600 nm) transitions of the Nd^{3+} ions were used for excitation and the fluorescence from the near-surface region of the sample was collected using the above signal detection arrangement. Slit widths of 150 μm, scanning step sizes of 0.2 nm and integration times of 0.5 s were adequate for the site-selective studies. Power values of 35 mW (near the sample) as well as same laser spot sizes were used in both excitation configurations. For life-time measurements, an optical chopper and a multi-channel analyzer were added to the PL set-up. To complement the emission characteristics of the Nd^{3+} ions doped into ZnO powders, an excitation spectrum was measured for each centre by scanning the dye laser through its lasing range while monitoring an isolated emission transition. Some temperature dependence studies were also conducted in the 20 – 75 K temperature range.

3. Results and discussion

Visual inspection of the powders at each stage of the sample preparation process showed distinct colour changes. The ZnO powder remained pure white after the grinding. However, the powder became off-white in colour following the compaction routine and then changed

back to pure white after the sintering. Such colour changes have been observed before for sintered ZnO powder samples [15]. In the case of doped powders, the off-green tint resulting from the blue Nd_2O_3 dopant deepened on co-doping with Li^+ ions. The relative densities of the samples, measured using the Archimedes principle, were found to be 92 ± 3 % which is considered acceptable for an adequately sintered sample [16].

3.1 Structural Characterization by Powder-XRD: PXRD patterns for the undoped, Nd-doped, Li-doped and Nd:Li co-doped ZnO powder samples sintered at 950 □ are presented in Fig. 1. In the undoped ZnO samples, diffraction peaks occur at 2θ = 37.14°, 40.23°, 42.38°, 55.87°, 66.84°, 74.57°, 78.96°, 80.95°, 82.44° and 86.85°. These were indexed to a single phase hexagonal wurtzite structure and correspond to the (100), (002), (101), (102), (110), (103), (200), (112), (201) and (004) Bragg planes, respectively [17]. No other chemical phases were formed on doping ZnO with Nd^{3+} and Li^+ ions. The diffraction patterns show increased relative intensities for peaks associated with the (002), (102) and (103) planes when Li^+ ions are added. This is an indication of changed preferential growth direction or texture formation [18].

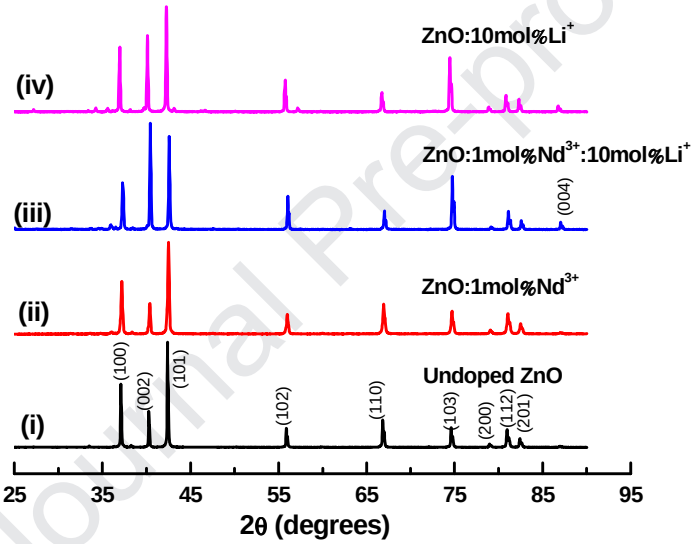

Figure 1 XRD patterns for undoped, 1mol%Nd^{3+} doped, 10mol%Li^+ doped and 1mol%Nd^{3+}:10mol%Li^+ co-doped ZnO powder samples sintered at 950 □ obtained with a cobalt radiation source of wavelength 0.179 nm. The corresponding planes are indicated in (i).

The lattice parameter values of a = 0.325 ± 0.001 nm and c = 0.521 ± 0.001 nm obtained here (Table 1) for ZnO powders (for bulk ZnO [19] a = 0.325 nm and c = 0.521 nm) are not affected by doping; this is plausible given the low concentration of the dopants and their ionic radii. Average crystallite sizes, S, determined using the Debye-Scherrer equation, are presented in the last column of Table 1. It can be seen that addition of Li_2CO_3 to either ZnO or ZnO:Nd^{3+} increases the sizes of the crystallites by about 90%. The Li_2CO_3, due to its low melting temperature (723 □), facilitates sintering and encourages grain growth by being the liquid-material in the liquid-phase sintering process [20].

Table 1 Peak positions of the (100) plane and the corresponding lattice parameters and crystallite sizes (S) for undoped, doped and co-doped ZnO powder samples sintered at 950 □.

Sample		Linewidth	Plane	Lattice parameters		
	2θ	(2θ)	spacing, *d*	*a*	*c*	S

	± 0.01 (˚)	± 0.02 (˚)	± 0.001 (nm)	± 0.001 (nm)	± 0.001 (nm)	± 0.2 (nm)
Undoped ZnO	37.14	0.09	0.281	0.325	0.520	132.1
ZnO:1mol%Nd^{3+}	37.21	0.09	0.281	0.325	0.520	140.0
ZnO:1mol%Nd^{3+}:10mol%Li^{+}	37.07	0.07	0.281	0.325	0.521	250.6
ZnO:10mol%Li^{+}	37.07	0.07	0.282	0.325	0.521	258.2

3.2 Surface morphology characterization by SEM: The surface morphologies of the ZnO:1mol%Nd^{3+}:10mol%Li^{+}, ZnO:10mol%Li^{+}, ZnO:1mol%Nd^{3+} and undoped ZnO powders are presented in Fig. 2 (a). Increased grain sizes in images (a)(i) and (a)(ii) are consistent with the larger crystallite sizes deduced from the XRD results (Table 1) on inclusion of Li_2CO_3. Additionally, the Nd^{3+} and Li^{+} co-doped sample ((a)(i)) showed tiny grains sparsely distributed in the boundary regions between the large grains.

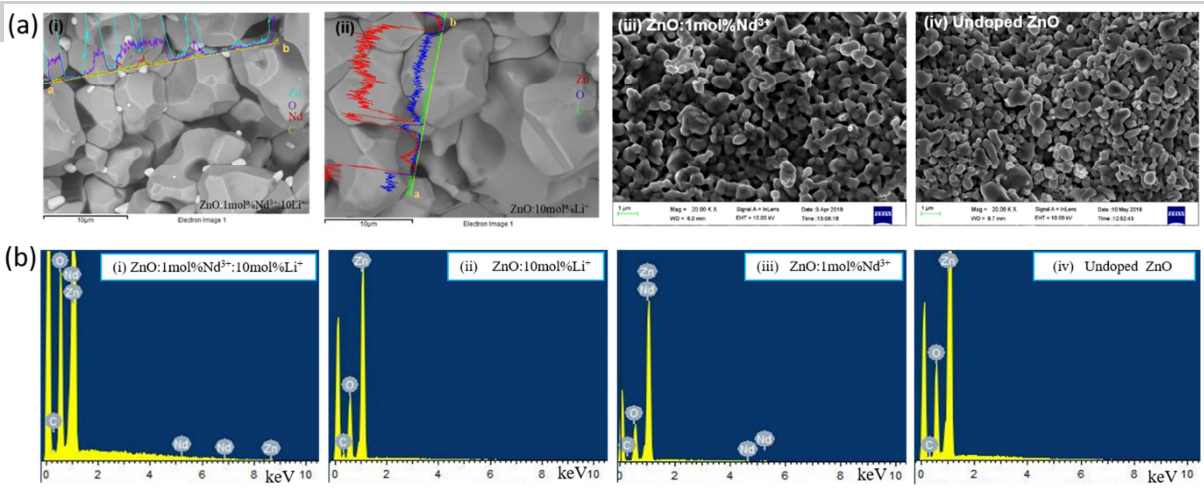

Figure 2 (a) SEM images and (b) EDS spectra for (i) 1mol%Nd^{3+}:10mol%Li^{+} co-doped, (ii) 10mol%Li^{+}-doped, (iii) 1mol%Nd^{3+}-doped, and (iv) undoped, ZnO powders sintered at 950 □. Line scans are included on the SEM images of the Li^{+}-doped samples (in (a) (i) and (ii)).

Typical elemental line scans for ZnO:1mol%Nd^{3+}:10mol%Li^{+} and ZnO:10mol%Li^{+} samples superposed on the SEM images in Fig. 2 (a)(i) and (a)(ii), respectively, show the distribution of constituent elements in the two samples containing Li^{+} ions. The Nd is not uniformly distributed across the surface of the sample, rather it is concentrated on the small grains within the boundary regions, where both Zn and O are in relatively low concentrations. This is consistent with reported observations [21] that RE^{3+} and Li^{+} ions associate with each other and are mainly located at the grain boundaries of ZnO. Migration of RE^{3+} and Li^{+} ions to the grain boundaries is caused by the lithium acting as an interstitial donor due to its high diffusion coefficient at the high sintering temperatures [22].

3.3 Compositional characterization by EDS: The EDS results presented in Fig. 2 (b) correspond to the SEM images in Fig. 2 (a). As expected, Nd^{3+} peaks were only detected in samples doped with Nd^{3+} ions ((i) and (iii)) with a ~ 60% increase in the amount of Nd detected in the Nd^{3+}:Li^{+} co-doped sample (spectrum (i)). Percentages of the constituent elements given on each spectrum are re-normalized to exclude the contribution which is mainly from the carbon tape (C) used to mount the sample. The detector generated reference peak appears at 0 keV. Li was not detected due to limited sensitivity of the EDS system to low atomic number elements.

3.4 Photoluminescence (PL)

Nd^{3+} emission was observed in Nd^{3+} and Li^{+} co-doped ZnO powder samples only, with both Ar^{+}-laser excitation at 457.9 nm and dye-laser excitation near 600 nm. The 457.9 nm (21 839 cm^{-1}) laser emission is not in near-resonance with any of the Nd^{3+} multiplet energy positions [12]. It is therefore expected that the laser radiation interacts with intrinsic ZnO defects such as zinc vacancies (V_{Zn}^{2-}) and interstitials (Zn_i^{+}), in the first instance. Energy levels for both intrinsic defects are in the 21 094 – 22 221 cm^{-1} energy range above the valence band maximum of ZnO and therefore overlap the incident photon energy. Subsequent energy transfer to Nd^{3+} ions results in observable emission in ZnO:1mol%Nd^{3+}:10mol%Li^{+} powders. The roles of alkali ions such as Li^{+} in the enhancement of rare-earth emission when co-doped with various rare-earth ions in different hosts are documented in the literature [14]. One of these is to provide charge compensation when a RE^{3+} ion (e.g. Nd^{3+}) substitutes a divalent ion

(e.g. Zn^{2+}). In this work, Nd^{3+} emission was observable only in samples co-doped with Nd^{3+} and Li^+ ions (Fig. 3) which supports the charge compensation role of Li^+ ions. This indicates that the incoming electromagnetic radiation interacts much more effectively with the Nd^{3+}-Li^+ dipole rather than with isolated Nd^{3+} ions. The higher Li^+ dopant concentration increases the probability of Li^+ ions occupying nearest neighbour and next nearest-neighbour lattice positions to Nd^{3+} ions, thereby increasing the concentration of such dipoles. A six-fold increase in Nd^{3+} emission intensity was realised on raising the Li^+ concentration from 1% to 5% while a 35% improvement resulted from further increase to 10% Li^+. This suggests that Li^+ saturation might occur just above 10mol% for the 1mol%Nd^{3+} dopant concentration (insert of Fig. 3). Hence,

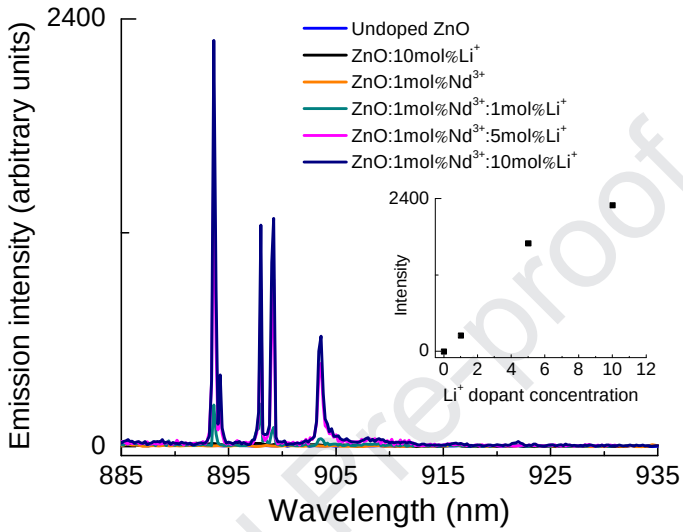

Figure 3 Nd^{3+}-emission spectra for ZnO:1mol%Nd^{3+}:xLi^+ (x = 0, 1, 5 and 10 mol%) powder samples measured at 10 K with the 457.9 nm excitation line. Spectra for undoped ZnO and ZnO:10mol%Li^+ powders are included for reference. Insert shows the Li^+ concentration dependence for the transition at 893.89 nm.

addition of Li^+ in commensurate quantities will enhance the Nd^{3+} emission significantly. The sharp emission lines in Fig. 3 correspond to the R ($^4F_{3/2}$) → Z ($^4I_{9/2}$) transitions of Nd^{3+} ions. To investigate the variety of Nd^{3+} centres present, the composite $^2G_{7/2}$;$^4G_{5/2}$ (D) Nd^{3+} multiplets accessible with the dye laser were directly excited in the ZnO:1mol%Nd^{3+}:10mol%Li^+ powder sample.

With the tunable dye laser, Z ($^4I_{9/2}$) → D ($^2G_{7/2}$;$^4G_{5/2}$) transitions are individually excited using the well-established technique of site-selective laser spectroscopy. For this procedure, the monochromator was set to 893.89 nm which coincides with the strongest emission transition (Fig. 3) obtained with Ar^+ laser excitation of the ZnO:1mol%Nd^{3+}:10mol%Li^+ sample. The dye-laser wavelength was then varied over the 570 – 640 nm range in order to determine excitation wavelengths that yield this particular emission transition. The excitation wavelength that results in strong emission was then used to obtain a characteristic (site-selective) emission spectrum. When the dye-laser excited emission spectrum was compared with the Ar^+-laser excited emission spectrum (Fig. 4 (a) and (b)), it was observed that the site-selective emission spectrum matched some but not all the Ar^+ laser excited emission transitions. The above process was then repeated with the monochromator set to 899.31 nm transition in the Ar^+-laser spectrum that was absent from the first site-selective emission spectrum. The resulting emission spectrum (Fig. 4 (c)) contained all the missing transitions only and so corresponds to a different Nd^{3+} site. The site-

selective emission spectra in Fig. 4 (b) and (c) are clearly different which shows that two distinct Nd^{3+} configurations (centres) co-exist in the powder samples. These have been arbitrarily labelled centre A and centre B corresponding to spectra (b) and (c) respectively, in Fig. 4. Dotted vertical lines shown in Fig. 4 guide the eye to the peak correspondence in spectra recorded with indirect (Ar^+ laser) and direct (dye-laser) excitation mechanisms.

Emission for both centres also falls in the 890 – 915 nm wavelength region associated with transitions from the $^4F_{3/2}$ (R) multiplet at ~895 nm to the ground $^4I_{9/2}$ (Z) multiplet. The emitting $^4F_{3/2}$ (R) multiplet of Nd^{3+} is some 5 300 cm^{-1} lower than the excited $^2G_{7/2}$;$^4G_{5/2}$ (D) multiplets and there are four intermediate multiplets ($^2H_{11/2}$ (C), $^4F_{9/2}$ (B), $^4F_{7/2}$;$^4S_{3/2}$ (A) and $^4F_{5/2}$;$^2H_{9/2}$ (S)). The inter-multiplet energy separation is ~1 000 cm^{-1} for any consecutive pair within this group and this can be bridged by creation of no more than two phonons, since the phonon cut-off energy is ~590 cm^{-1} for ZnO. The corresponding non-radiative relaxation rate for Nd^{3+} doped oxides is ~10^7 s^{-1} [23], which is quite high, and so the $^4F_{3/2}$ (R) multiplet is efficiently populated by a cascade process.

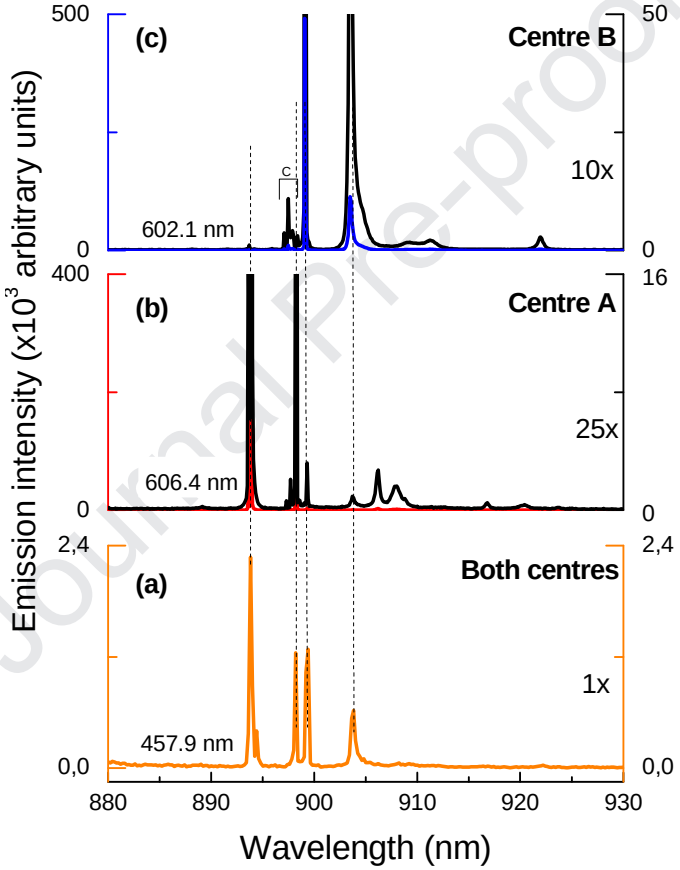

Figure 4 Emission spectra for ZnO:1mol%Nd^{3+}:10mol%Li^+ powder samples sintered at 950 □ recorded at 10 K with (a) indirect excitation at 457.9 nm and direct excitation at (b) 606.40 nm and (c) 602.10 nm, respectively. Spectra (b) and (c) have been magnified by 25x and 10x, respectively.

It can be seen in Fig. 4 that the main transitions of centres A and B in the 892 – 905 nm region account for all the Ar^+-laser excited transitions; the Ar^+ laser therefore simultaneously activates the different Nd^{3+} centres but distinction is not possible. The emission intensity is three orders of magnitude higher when the Nd^{3+} ions are excited directly than when indirectly excited below the conduction band, under the same experimental conditions. The centre A and centre B emission spectra also show weaker multiple peaks in the 897 – 900 nm region,

labelled C in Fig. 4 (c); these peaks could arise from Nd^{3+} clusters within the lattice. The intense and well resolved Nd^{3+} emission lines are consistent with well-ordered crystal-field surroundings of the Nd^{3+} ions [2]. While the composite emission spectrum due to multiple different centres that is obtained via excitation of intrinsic defects (Fig. 4 (a)) has been reported before [2,3,21], to the best of our knowledge, this study is the first reported attempt at distinguishing and characterizing emission from different Nd^{3+} centres in ZnO powders.

For a rare-earth ion with an odd number of 4*f* electrons such as Nd^{3+}, Kramer's degeneracy leads to $J+^1/_2$ doubly degenerate crystal-field energy levels for each of the $^{2S+1}L_J$ multiplets, in any sub-cubic symmetry environment. In ZnO, the Zn^{2+} ion site is of C_{3v} symmetry. Substitution of two neighbouring Zn^{2+} ions by Nd^{3+} and Li^+ ions reduces the symmetry at the Nd^{3+} site to an extent depending on the Li^+ ion relative position and the overall local distortion. In any case, inter-multiplet transitions between any two crystal-field levels are

allowed because of the random orientations of the Nd^{3+}-Li^+ induced dipoles in the powder sample, relative to the plane-polarized incident laser radiation. There are five crystal-field levels in the Z ($^4I_{9/2}$) multiplet, two in the R ($^4F_{3/2}$) multiplet and seven (4 + 3) in the dye-laser excited D ($^2G_{7/2}$;$^4G_{5/2}$) multiplet of Nd^{3+} [12,24]. As such ten transitions are possible between the $^4F_{3/2}$ and $^4I_{9/2}$ multiplets of Nd^{3+}, for example. Statistically, only energy levels within energy $\Delta E \cong kT$ (k is Boltzmann's constant and T is temperature in kelvins) above the lowest energy level in an excited multiplet can be sufficiently populated at temperature T to contribute to emission. At 10 K, $\Delta E \cong 7$ cm^{-1}. As the temperature is raised, transitions from the higher lying levels of the excited multiplet grow in intensity at the expense of the low temperature (10 K) transitions. Such considerations enable distinction between emission transitions emanating from the lowest energy crystal-field level and those originating from higher-lying levels of the same multiplet. Following this line of reasoning, all the Nd^{3+} ion emission transitions present at 10 K (Fig. 4 (b) and (c)) therefore originate from the lower level (R_1) of the $^4F_{3/2}$ multiplet to each of the Z_1 to Z_5 levels of the ground multiplet ($^4I_{9/2}$). Further, spectra recorded at the higher temperatures of 20 K, 50 K and 75 K for the two centres, presented in Fig. 5 enable identification of emission transitions originating from the higher-lying energy level, R_2, of the $^4F_{3/2}$ multiplet to the ground multiplet crystal-field levels. All the electronic transitions observed for the two centres are presented in Table 2 and the resulting relative crystal-field energy level positions in Table 3. The $R_1 \rightarrow Z_1$ emission transition is dominant in each centre spectrum, with comparable intensities. In addition, the transition shifts to slightly higher wavelengths as the sample temperature is raised, for both centres. At 75 K, the shift is 0.18 nm (2.0%) for centre A and 0.15 nm (1.7%) for centre B. In comparison, the spectral position of the second most intense transition ($R_1 \rightarrow Z_2$) remains unchanged in both cases. In general, sharp spectral transitions exhibit a red shift in wavelength or energy position as the temperature of the sample is raised [25,26]. The shifts to lower energies (higher wavelengths) are due to the dynamic strain induced by lattice vibrations in the vicinity of the emitting ion. Normally, the downward shift in energy position is larger for crystal-field energy levels in the higher lying multiplets in comparison to the ground multiplet levels [25,26], resulting in an overall decrease in the transition energy, as observed here for the $R_1 \rightarrow Z_1$ transitions. However, it can happen that some crystal-field levels in the ground $^4I_{9/2}$ (Z) multiplet and first excited $^4I_{9/2}$ (Y) multiplet undergo unusually large shifts to lower energies resulting in insignificant overall changes to

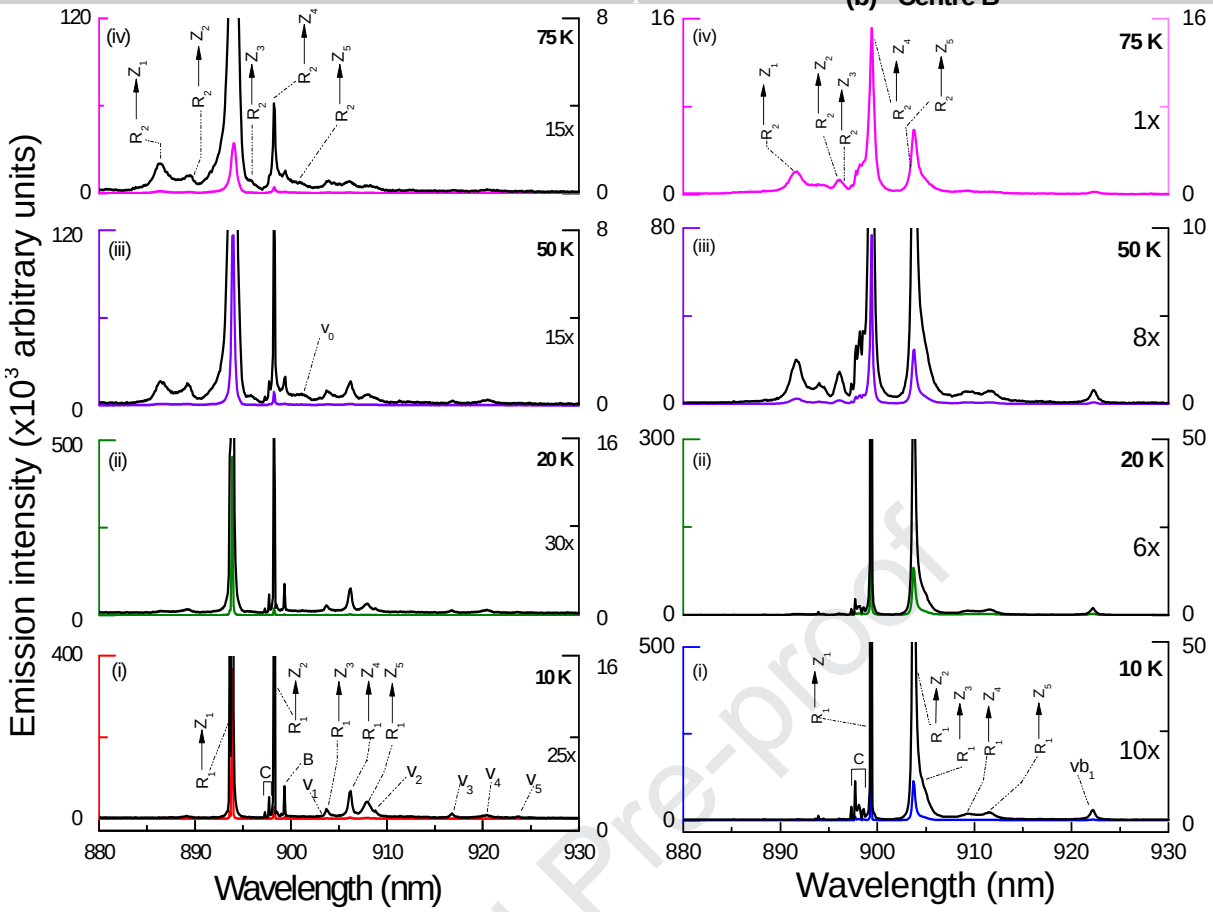

Figure 5 Emission spectra for (a) centre A and (b) centre B in ZnO:1mol%Nd^{3+}:10mol%Li^{+} powder samples sintered at 950 □, obtained with excitation at 606.40 nm and 602.10 nm, respectively. Transitions from the R_1 and R_2 crystal-field levels of the R ($^4F_{3/2}$) multiplet to the Z ($^4I_{9/2}$) multiplet crystal-field levels (Z_1 to Z_5) are identified in the 10 K and 75 K spectra, respectively. Vibronic transitions are labelled v_j (j = 0 – 5) in (a) and vb_1 in (b). B and C identify breakthrough emission from centre B and the cluster centre(s), respectively.

the transition positions, as is the case here for the $R_1 \rightarrow Z_2$ transitions. Similarly negligible shifts have been reported for the $R_{1,2} \rightarrow Y_6$ transitions of Nd^{3+} doped garnets [13] while a blue shift is clearly apparent for the $R_1 \rightarrow Z_5$ transition [13,25,26]. This anomalous behaviour is accounted for by the 'pushing down' of the highest crystal-field level of the ground multiplet (Z_5) and the first-excited multiplet (Y_6) by the nearest higher energy Y and X multiplets, respectively. For both the ZnO:Nd^{3+}:Li^{+} centres reported here, the $R_1 \rightarrow Z_{3,4,5}$ transitions were too weak and broad for any discernible shifts in position. However, a blue-shifted $R_1 \rightarrow Z_5$ transition, is entirely consistent with the negligible shift observed here for the $R_1 \rightarrow Z_2$ transition, since the Z_1 level sets the lower limit.

The $Z_1 - Z_5$ energy spread of the ground multiplet ($^4I_{9/2}$) is ~180 cm^{-1} for centre A and ~150 cm^{-1} for centre B while the $Z_1 - Z_2$ separation is common (54.2 cm^{-1}) (Table 3). Weaker vibronic features are labelled $v_0 - v_5$ for centre A and vb_1 for centre B in Fig. 5 (a) and (b), respectively. The corresponding phonon modes are identified in Table 4.

Table 2 Peak positions and electronic transition assignments for centre A and centre B in the ZnO:1mol%Nd^{3+}:10mol%Li^{+} powder sample.

	Centre A peak position	Centre B peak position	Corresponding

Inter-multiplet transitions	Sample temperature	Wavelength (± 0.01 nm)	Energy (± 0.1 cm^{-1})	Wavelength (± 0.01 nm)	Energy (± 0.1 cm^{-1})	electronic transition
		893.89	11 187.1	899.31	11 119.6	$R_1 \rightarrow Z_1$
		898.24	11 132.9	903.72	11 065.4	$R_1 \rightarrow Z_2$
	10 K	903.73	11 065.2	904.43	11 056.7	$R_1 \rightarrow Z_3$
		905.94	11 038.2	909.45	10 995.7	$R_1 \rightarrow Z_4$
R ($^4F_{3/2}$) → Z ($^4I_{9/2}$)		907.93	11 014.0	911.49	10 971.1	$R_1 \rightarrow Z_5$
		886.38	11 281.8	891.71	11 214.4	$R_2 \rightarrow Z_1$
emission transitions		890.66	11 227.6	896.04	11 160.2	$R_2 \rightarrow Z_2$
	75 K	896.06	11 159.9	896.74	11 151.5	$R_2 \rightarrow Z_3$
		898.24	11 132.9	901.67	11 090.5	$R_2 \rightarrow Z_4$
		900.19	11 108.7	903.68	11 065.9	$R_2 \rightarrow Z_5$
		606.32	16 492.8	609.27	16 413.1	$Z_1 \rightarrow D_1$
		600.53	16 651.9	601.99	16 611.6	$Z_1 \rightarrow D_2$
		597.70	16 730.8	600.74	16 646.0	$Z_1 \rightarrow D_3$
	10 K	590.16	16 944.5	593.13	16 859.6	$Z_1 \rightarrow D_4$
		589.49	16 963.9	591.33	16 911.1	$Z_1 \rightarrow D_5$
		586.52	17 049.6	589.28	16 969.9	$Z_1 \rightarrow D_6$
		582.35	17 171.8	584.56	17 106.8	$Z_1 \rightarrow D_7$
Z ($^4I_{9/2}$) → D ($^2G_{7/2}$; $^4G_{5/2}$)		611.29	16 358.9	608.32	16 438.6	$Z_2 \rightarrow D_1$
		603.96	16 557.4	--	--	$Z_2 \rightarrow D_2$
		602.71	16 591.8	--	--	$Z_2 \rightarrow D_3$
excitation transitions		--	--	--	--	$Z_2 \rightarrow D_4$
		593.23	16 856.9	--	--	$Z_2 \rightarrow D_5$
		591.17	16 915.7	588.39	16 995.4	$Z_2 \rightarrow D_6$
	75 K	586.42	17 052.6	584.19	17 117.6	$Z_2 \rightarrow D_7$
		611.61	16 350.2	610.84	16 370.9	$Z_3 \rightarrow D_1$
		604.28	16 548.7	604.96	16 530.0	$Z_3 \rightarrow D_2$
		603.02	16 583.1	602.09	16 608.9	$Z_3 \rightarrow D_3$
		--	--	586.51	17 049.9	$Z_3 \rightarrow D_7$

Site-selective excitation spectra were obtained by scanning the dye laser over the dye range (570 – 640 nm) whilst separately monitoring the strongest transition ($R_1 \rightarrow Z_1$) of each centre and the results are presented in Fig. 6. Spectra (ii)-(iv) show variations in the excitation transitions for the two centres, with increasing sample temperature. The $Z_2 \rightarrow D$ and $Z_3 \rightarrow D$ transitions grow with temperature. All the excitation transitions present in the 10 K spectra are expected to be from the lowest crystal-filed level (Z_1) of the ground multiplet ($^4I_{9/2}$) to the seven crystal-filed levels of the excited D ($^2G_{7/2}$;$^4G_{5/2}$) multiplet, given that the $Z_1 – Z_2$ separation (54.2 cm^{-1}) is greater than kT. The $Z_1 \rightarrow D_i$ (i = 1 – 7) transitions are identified on spectra (a)(i) and (b)(i) of Fig. 6 while the observable $Z_{2,3} \rightarrow D_i$ transitions are shown in the 75 K spectra (a)(iv) and (b)(iv); these are included in Table 2. Because of the smaller $Z_2 – Z_3$ separation for centre B, the $Z_3 \rightarrow D$ transitions always appear as shoulders to the $Z_2 \rightarrow D$ transitions (spectrum (b)(iv) in Fig. 6); the separation between the Z_2 and Z_3 energy levels is about 70 cm^{-1} for centre A and only 15 cm^{-1} for centre B. Also, the $^4F_{3/2}$ multiplet for the centre A is at about 70 cm^{-1} higher than that for the centre B. Both pairs of levels of the $^4F_{3/2}$ multiplet are separated by about 95 cm^{-1}. The deduced energy positions of levels in the excited D ($^2G_{7/2}$;$^4G_{5/2}$) multiplet are included in Table 3. Additional peaks labelled w_i (i = 1 – 6) in spectrum (a)(iii) and y_i (i = 1, 2, 3) in spectrum (b)(i) of Fig. 6 associated with phonon modes of the lattice are included in Table 4. Peaks identified with C can be related to the cluster centre(s) which give the weak emission at ~898 nm in Fig. 5.

Table 3 Crystal-field energy levels for the Z ($^4I_{9/2}$) and R ($^4F_{3/2}$) and D ($^2G_{7/2}$;$^4G_{5/2}$) multiplets of the two Nd^{3+} centres in ZnO:1mol%Nd^{3+}:10mol%Li^+ powders.

	Energy levels
	Energy (± 0.1cm^{-1})

Multiplet	Label	Centre A	Centre B
Z	Z_1	0.0	0.0
($^4I_{9/2}$)	Z_2	54.2	54.2
	Z_3	121.9	69.2
	Z_4	148.9	123.9
	Z_5	173.1	148.5
R	R_1	11 187.1	11 119.6
($^4F_{3/2}$)	R_2	11 281.8	11 214.4
D	D_1	16 492.8	16 413.1
($^2G_{7/2}$;$^4G_{5/2}$)	D_2	16 651.9	16 611.6
	D_3	16 730.8	16 646.0
	D_4	16 944.5	16 859.6
	D_5	16 963.9	16 911.1
	D_6	17 049.6	16 969.9
	D_7	17 171.8	17 106.8

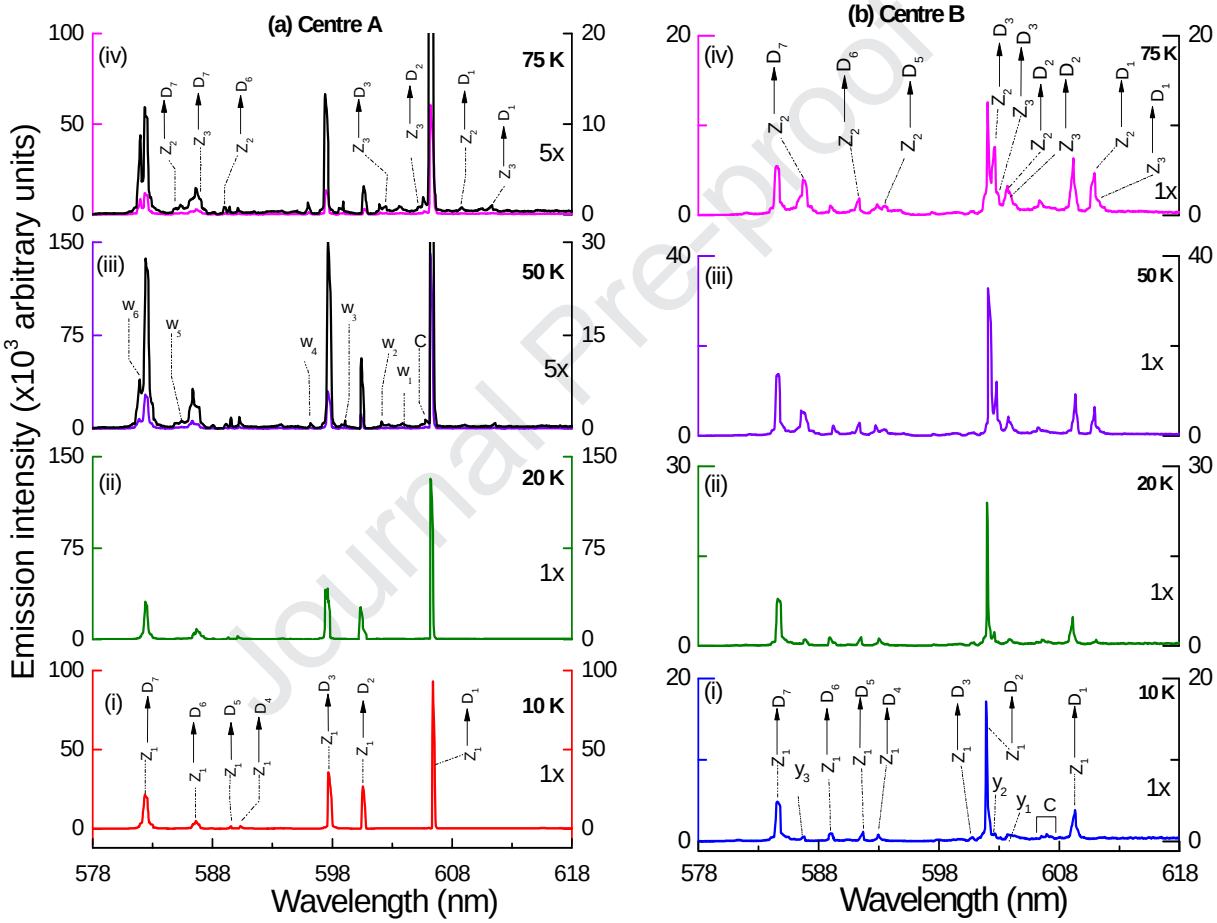

Figure 6 Excitation spectra for (a) centre A and (b) centre B in ZnO:1mol%Nd^{3+}:10mol%Li^+ powder samples sintered at 950 □, measured in the 10 K – 75 K temperature range, while monitoring the $R_1 \rightarrow Z_1$ transition at 893.89 nm and 899.31 nm, respectively. Transitions from Z_1 and the higher Z levels (Z_2, Z_3) to the D multiplet crystal-field levels (D_1 to D_7) are identified in the 10 K and 75 K spectra, respectively. Vibronic transitions are labelled w_i (i = 1 – 6) and y_i (i = 1, 2, 3) while C identifies cluster centre transitions.

Table 4 Vibronic transitions and the associated electronic transitions as well as the corresponding phonon modes for the R → Z emission and Z → D excitation transitions of

centre A and centre B in ZnO:1mol%Nd^{3+}:10mol%Li^{+} powder samples. The transitions are identified in Fig. 5 and Fig. 6.

Centre and Label	Electronic transitions		Associated vibronic transitions			Phonons	
	Wavelength (± 0.01 nm)	Energy (± 0.1 cm^{-1})	Label	Wavelength (± 0.01 nm)	Energy (± 0.1 cm^{-1})	Energy (± 0.2 cm^{-1})	Modes
Centre A							
$R_1 \rightarrow Z_1$	893.89	11 187.1	v_0	900.58	11 104.0	83.1	TA (A) [27]
			v_1	902.68	11 078.1	109.0	TA(M) [28,29]
			v_2	908.78	11 003.8	183.3	TA (A) [27,28]
			v_3	916.82	10 907.3	279.8	LA (M) [28]
			v_4	920.32	10 865.8	321.3	$3 \times v_1$
			v_5	923.61	10 827.1	360.0	$2 \times v_2$
$Z_1 \rightarrow D_1$	606.32	16 492.8	w_1	603.29	16 575.9	83.1	TA (A) [27]
			w_2	601.87	16 614.9	122.1	TA(M) [27]
			w_3	598.87	16 698.2	205.4	$w_1 + w_2$
			w_4	596.15	16 774.4	281.6	LA (M) [28]
$Z_1 \rightarrow D_3$	597.70	16 730.8	w_5	585.43	17 081.4	588.6	LO (Γ) [30]
			w_6	582.00	17 182.0	451.2	TO (M) [27]
Centre B							
$R_1 \rightarrow Z_1$	899.31	11 119.6	vb_1	922.13	10 844.4	275.2	LA (M) [28]
$Z_1 \rightarrow D_1$	609.27	16 413.1	y_1	604.17	16 551.5	138.4	TA(M) [28,29]
			y_2	602.85	16 587.9	174.8	TA (A) [27,28]
$Z_1 \rightarrow D_2$	601.99	16 611.6	y_3	586.32	17 055.6	444.0	TO (M) [29]

3.5 Life-time studies

Although, the emission life-time of the $^4F_{3/2}$ multiplet has been reported for Nd^{3+} ions doped into different ZnO powders [2], there was no distinction between the two different Nd^{3+} centres. In our work, the life-time for each centre was separately measured. The $R_1 \rightarrow Z_1$ transition peaks at 893.89 nm and 899.31 nm were monitored for the measurements while dye-laser wavelengths of 606.40 nm and 602.10 nm were used for exciting centres A and B, respectively. Exponential decay curves of the form $y = A \exp(-t/\tau) + y_0$ fitted to the recorded data yield the life-time (τ) of centre A as 202 ± 4 μs whilst that for centre B is 380 ± 4 μs. Liu *et al.* [2]. reported room-temperature life-times ranging from 22 μs to 358 μs from composite decay curves. At room temperature, the emission transitions are very much broadened and therefore overlap, leading to unintentional simultaneous excitation of neighbouring transitions that belong to different centres. Although the resulting decay curve is a composite of two decay curves, it can still be fitted to a single exponential curve since the lifetimes are of the same order of magnitude. The fact that the Liu *et al.* values (328 μs and 358 μs) [2] are somewhat less than our value for the B centre (380 μs) is an indication that the B centre transition that was excited overlaps an A centre transition to some degree at the chosen excitation wavelength. Meanwhile, the fast life-times (<120 μs) could be for clustered rather than isolated Nd^{3+} ions.

3.6 Defect configurations

Atomistic modelling calculations have been performed to help identify centres A and B. The calculations were performed using the GULP code [31], with interionic potentials defined for the ZnO lattice, and for the interactions of Nd^{3+} and Li^{+} ions with the host lattice. The potentials used take the Buckingham form: $V(r) = A \exp(-r/\rho) - Cr^{-6}$. Potential parameters are listed in Table 5.

Table 5 Potential parameters for ZnO and Nd, Li interactions

Interaction	A (eV)	ρ (Å)	C (eV Å^6)
Zn-O	499.6	0.3595	0.0
O-O	22764.0	0.149	20.37
Nd-O	1989.20	0.3430	22.59
Li-O	950.00	0.261	0.0

Formal charges were used for all ions, and a shell model employed for O, with shell charge Y = -2 |e| and spring constant k = 15.52 eV Å^{-2}.

Defect configurations were modelled using a supercell approach, chosen to ensure that a range of ion positions are available. In the method, the centre formation energy is calculated by taking the difference between the energy of the supercell with the centre, and the perfect supercell. An example of the application of this method is available for Pu-doped UO_2 [32]. Using this method, the formation energy for a range of centres involving Nd^{3+} and Li^{+} ions in ZnO have been calculated, and these are given in Table 6. In each case, the Nd^{3+} and Li^{+} ions replace Zn^{2+} ions in the lattice, forming charge-neutral centres. Here, the two basis Zn^{2+} positions for the wurtzite ZnO lattice with coordinates (1/3,2/3,0) and (2/3,1/3,1/2) [19] are labelled positions 1 and 4, respectively in Fig. 7. Positions 2 and 3 fall outside the supercell, hence symmetrically equivalent positions (marked 2* and 3*) were used. From the table it is clear that the centres 5-2* and 5-3* have the lowest formation energy, and may correspond to the experimentally determined centres A and B. The common defect formation energy is consistent with the comparable emission intensities.

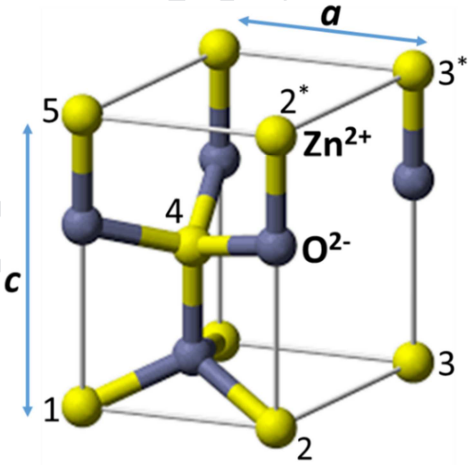

Figure 7 The hexagonal wurtzite structure of ZnO showing Zn^{2+} ion positions 1-5, 2^* and 3^* used in calculations.

Table 6 Formation energies of Nd-Li centres in ZnO. Positions are as shown in Fig. 7.

Nd position	Li position	Defect formation energy (eV)
1/3, 2/3, 0 (position 1)	1/3, 2/3, 1 (position 5)	0.23
1/3, 2/3, 0 (position 1)	2/3, 1/3, 0.5 (position 4)	0.12
1/3, 2/3, 0 (position 1)	4/3, 5/3, 1 (position 3*)	0.50
1/3, 2/3, 1 (position 5)	4/3, 5/3, 1 (position 3*)	0.11
1/3, 2/3, 1 (position 5)	4/3, 2/3, 1 (position 2*)	0.11
2/3, 1/3, 0.5 (position 4)	4/3, 5/3, 1 (position 3*)	0.75
2/3, 1/3, 0.5 (position 4)	4/3, 2/3, 1 (position 2*)	0.12

4. Conclusions

Two distinct Nd^{3+} centres were identified in ZnO:1mol%Nd^{3+}:10mol%Li^{+} powders sintered at 950 □ and their spectral and temporal characteristics for the $^4F_{3/2} \rightarrow {}^4I_{9/2}$ emission and $^4I_{9/2} \rightarrow {}^2G_{7/2};{}^4G_{5/2}$ excitation transitions documented. Judging from peak emission intensities, both centres have more than 95% of their energies in one transition ($R_1 \rightarrow Z_1$), a characteristic which would be useful in monochromatic laser applications. Calculations show that the two most likely Nd^{3+}-Li^{+} defect configurations in ZnO are the nearest neighbour and next nearest neighbour Zn^{2+} positions in the (0001) basal plane.

Acknowledgements

Technical assistance from Mr. S. Masina and Mr. B. N. Nelelwani is greatly acknowledged.

Funding

This work was funded by African Materials Science and Engineering Network, AMSEN (a Carnegie-IAS RISE Network). Financial support was also provided by DST/NRF Centre of Excellence in Strong Materials and the University of the Witwatersrand, Johannesburg through research grants.

References

1. D. Daksh, Y.K. Agrawal, Rare earth-doped zinc oxide nanostructures: A review, Rev. Nanosci. Nanotechnol. 5 (2016) 1–27. doi:10.1166/rnn.2016.1071.
2. Y. Liu, W. Luo, R. Li, H. Zhu, X. Chen, Near-infrared luminescence of Nd^{3+} and Tm^{3+} ions doped ZnO nanocrystals, Opt. Express. 17 (2009) 9748–9753. doi:10.1364/OE.17.009748.
3. Y. Liu, W. Luo, R. Li, X. Chen, Optical properties of Nd^{3+} ion-doped ZnO nanocrystals, J. Nanosci. Nanotechnol. 10 (2010) 1871–1876. doi:10.1166/jnn.2010.2140.
4. M. Balestrieri, S. Colis, M. Gallart, G. Ferblantier, D. Muller, P. Gilliot, P. Bazylewski, G.S. Chang, A. Slaoui, A. Dinia, Efficient energy transfer from ZnO to Nd^{3+} ions in Nd-doped ZnO films deposited by magnetron reactive sputtering, J. Mater. Chem. C. 2 (2014) 9182–9188. doi:10.1039/C4TC00980K.
5. A. Manikandan, E. Manikandan, B. Meenatchi, S. Vadivel, S.K. Jaganathan, R. Ladchumananandasivam, M. Henini, M. Maaza, J.S. Aanand, Rare earth element (REE) lanthanum doped zinc oxide (La: ZnO) nanomaterials: Synthesis structural optical and antibacterial studies, J. Alloys Compd. 723 (2017) 1155–1161. doi:10.1016/j.jallcom.2017.06.336.
6. V. Kumar, O.M. Ntwaeaborwa, T. Soga, V. Dutta, H.C. Swart, Rare earth doped zinc oxide nanophosphor powder: A future material for solid state lighting and solar cells, ACS Photonics. 4 (2017) 2613–2637. doi: 10.1021/acsphotonics.7b00777.
7. A. Layek, S. Banerjee, B. Manna, A. Chowdhury, Synthesis of rare-earth doped ZnO nanorods and their defect–dopant correlated enhanced visible- orange luminescence, RSC Adv. 6 (2016) 35892–35900. doi:10.1039/C6RA02278B.
8. K.S. Yu, J.Y. Shi, Z.L. Zhang, Y.M. Liang, W. Liu, Synthesis, characterization, and photocatalysis of ZnO and Er-Doped ZnO, J. Nanomater. 2013 (2013) 1–6. doi:10.1155/2013/372951.
9. S.D. Barrett, S.S. Dhesi, Introduction to the rare earths, in: Struct. Rare-Earth Met. Surfaces, Imperial College Press, London, 2001: pp. 1–19.
10. H. Morkoç, Ü. Özgür, Zinc Oxide: fundamentals, materials and device technology, Wiley-VCH Verlag GmbH & Co. KGaA, 2009.
11. P. Rong, S. Ren, Q. Yu, Fabrications and Applications of ZnO Nanomaterials in Flexible Functional Devices - A Review, Crit. Rev. Anal. Chem. 49 (2019) 336–349. doi:10.1080/10408347.2018.1531691.
12. S. Hufner, Optical Spectra of Transparent Rare Earth Compounds, Academic Press, Inc, New York, United States, 1978. doi:10.1063/1.2995463.

13. X. Chen, B. Di Bartolo, Phonon effects on sharp luminescence lines of Nd^{3+} in $Gd_3Sc_2Ga_3O_{12}$ garnet (GSGG), J. Lumin. 54 (1993) 309–318.
14. A.K. Singh, S.K. Singh, S.B. Rai, Role of Li^+ ion in the luminescence enhancement of lanthanide ions: favorable modifications in host matrices, RSC Adv. 4 (2014) 27039–27061. doi:10.1039/c4ra01055h.
15. T. J. Gray, Sintering of zinc oxide, J. Am. Ceram. Soc. 37 (1954) 534–538. doi:10.1111/j.1151-2916.1963.tb11774.x.
16. Z. Zak Fang, Sintering of advanced materials: fundamental and processes, Cambridge, UK: Woodhead Publishing Limited, 2010.
17. L. Lin, Y. Han, M. Fuji, T. Endo, X. Wang, M. Takahashi, Synthesis of hexagonal ZnO microtubes by a simple soft aqueous solution method, J. Ceram. Soc. Japan. 116 (2008) 198–200. doi:10.2109/jcersj2.116.198.
18. F. Solís-Pomar, E. Martínez, M.F. Meléndrez, E. Pérez-Tijerina, Growth of vertically aligned ZnO nanorods using textured ZnO films, Nanoscale Res. Lett. 6 (2011) 524–535. doi:10.1186/1556-276X-6-524.
19. E.H. Kisi, M.M. Elcombe, u parameters for the wurtzite structure of ZnS and ZnO using powder neutron diffraction, Acta Crystallogr. Sect. C Cryst. Struct. Commun. 45 (1989) 1867–1870. doi:10.1107/s0108270189004269.
20. M.N. Rahaman, Ceramic Fabrication Processes, in: Ceram. Process. Sinter., 2nd ed., Marcel Dekker, Inc, New York, United States, 2003: pp. 1–44.
21. W.M. Jadwisienczak, H.J. Lozykowski, A. Xu, B. Patel, Visible emission from ZnO doped with rare-earth ions, J. Electron. Mater. 31 (2002) 776–784. doi:10.1007/s11664-002-0235-z
22. J.J. Lander, Reactions of Lithium as a donor and an acceptor in ZnO, J. Phys. Chem. Solids. 15 (1960) 324–334. doi:10.1016/0022-3697(60)90255-9.
23. T.T. Basiev, A.Y. Dergachev, Y. V. Orlovskii, A.M. Prokhorov, Multiphonon nonradiative relaxation from high-lying levels of Nd^{3+} ions in flouride and oxide laser materials, J. Lumin. 53 (1992) 19–23. doi:10.1016/0022-2313(92)90096-R.
24. B.G. Wybourne, Spectroscopic Properties of Rare Earths, Interscience Publishers- John Wiley & Sons. Inc., 1965. doi:10.1126/science.148.3673.1082.
25. D.K. Sardar, S.C. Stubblefield, Temperature dependencies of linewidths, positions, and line shifts of spectral transitions of trivalent neodymium ions in barium magnesium yttrium germanate laser host, J. Appl. Phys. 83 (1998) 1195–1199. doi:10.1063/1.366815.
26. T. Kushida, Linewidths and thermal shifts of spectral lines in neodymium-doped yttrium aluminum garnet and calcium fluorophosphate, Phys. Rev. 185 (1969) 500–508. doi:10.1103/PhysRev.185.500.
27. J. Serrano, F.J. Manjón, A.H. Romero, A. Ivanov, M. Cardona, R. Lauck, A. Bosak, M. Krisch, Phonon dispersion relations of zinc oxide: Inelastic neutron scattering and ab initio calculations, Phys. Rev. B. 81 (2010) 174304–9. doi:10.1103/PhysRevB.81.174304.
28. U.G. Kaufmann, P. Koidl, Jahn-Teller effect in the $^3T_1$ (P) absorption band of Ni^{2+} in ZnS and ZnO, J. Phys. C Solid State Phys. 7 (1974) 791–806. doi: 10.1088/0022-3719/7/4/015
29. S. S. Mitra, R. Marshall, Multiphonon infrared absorption in II-VI semiconductors, in: 7th Int. Conf. Phys. Semicond., 1963: pp. 1085–1090.
30. C. Bundesmann, N. Ashkenov, M. Schubert, A. Rahm, H. V. Wenckstern, E.M. Kaidashev, M. Lorenz, M. Grundmann, Infrared dielectric functions and crystal orientation of a-plane ZnO thin films on r-plane sapphire determined by generalized ellipsometry, Thin Solid Films. 455 (2004) 161–166. doi:10.1016/j.tsf.2003.11.226.
31. J.D. Gale, GULP: A computer program for the symmetry-adapted simulation of solids, J. Chem. Soc., Faraday Trans. 93 (1997) 629–637. doi:10.1039/A606455H
32. R.A. Jackson, J.E. Huntingdon, R.G.J. Ball, Defect Calculations in Solids beyond the dilute limit, J. Mater. Chem. 1 (1991) 1079–1080. doi:10.1039/jm9910101079.

Highlights

- Structure and surface morphology of sintered ZnO:Nd^{3+}:Li^{+} powders were determined
- Spectroscopy of the two Nd^{3+}-Li^{+} centres present in ZnO powders is presented
- Crystal-field levels for $^{2}G_{7/2}$;$^{4}G_{5/2}$, $^{4}F_{3/2}$ and $^{4}I_{9/2}$ multiplets of Nd^{3+} were deduced
- Proposed centre configurations were obtained from modelling calculations

Declaration of interests

☒ The authors declare that they have no known competing financial interests or personal relationships that could have appeared to influence the work reported in this paper.

☐The authors declare the following financial interests/personal relationships which may be considered as potential competing interests: